Final submitted manuscript: published in Journal of Sound and Vibration [accepted 6/11/21]
doi: 10.1016/j.jsv.2021.116620

Wave interference in railway track due to multiple wheels

Simian Lei[1], Yaojun Ge[1], Qi Li[1*], David J. Thompson[2]

[1] Department of Bridge Engineering, Tongji University

1239 Siping Road, Shanghai, China

[2] Institute of Sound and Vibration Research, University of Southampton,

Southampton SO17 1BJ, United Kingdom

Highlights

1. Reveal the nature of the boundary conditions provided by wheels mounted on the track

2. Explain the generation of multiple peaks in track vibration based on phase closure

3. Explain the highest response peak around 700 Hz due to total reflection at the wheels

Abstract

A resonance pattern at frequencies from around 400 Hz to 1000 Hz has often been observed from measured rail accelerations. Such resonances are important for rail noise and corrugation. Although this pattern has been reported and discussed in several papers in terms of wave reflections between multiple wheels, the aim of this study is to investigate the generation mechanism of this resonance phenomenon in detail, and to give both mathematical and physical insight. An infinite Timoshenko beam with continuous supports is adopted for modelling the track system, and the point and

transfer receptances of the rail for a stationary harmonic excitation are explicitly obtained by the residue theorem. A frequency-domain method is then presented to calculate the power spectral densities of the wheel-track coupled system responses to stochastic irregularities with the moving irregularity model. It is found that the multiple peaks can be explained by using the phase closure principle. Moreover, total reflection between the two wheels may occur at around 700 Hz, which results in the highest peak in the response.

Keywords

Railway track; wheel-rail interaction resonance; reflection and transmission ratio; phase closure principle; track irregularity.

1 Introduction

Dynamic wheel-rail interactions in the railway system are mainly caused by the irregular profiles on the wheel and rail contact surfaces, among which random track undulations (also called track geometry irregularities or rail roughness) are the major source. If the responses of the train-track coupled system induced by track irregularities are presented in the frequency domain, they contain several peaks at different frequencies associated with various mechanisms, such as system resonances [1]. These peaks in the vibration spectra of the wheel and rail may result in higher environmental noise at particular frequencies, from dozens to thousands of Hertz [2, 3], negatively affecting the comfort of both passengers and residential areas as trains pass by. Besides, the high frequency wheel-rail contact forces play an important role in the formation of

railhead corrugation [4], which in turn causes increased wheel-rail interaction forces. In view of these considerable effects, many attempts have been made to investigate the origin of the dominant peaks in the wheel-rail interaction forces and the vibration of the train-track system.

Typical natural frequencies of the car bodies and bogies on the suspension system usually lie below 10 Hz [5, 6], whereas the first bending mode of the axles occurs at around 100 Hz [7]. The track also has a number of resonances. A ballasted track has a highly damped resonance at about 100 Hz related to the total track mass bouncing on the stiffness of the ballast [8]; slab tracks have a similar, but more lightly damped, resonance due to the flexibility of the rail fasteners. For a track with sleepers mounted in ballast or on elastic supports, an anti-resonance of the track occurs at about 200-300 Hz caused by the sleepers vibrating between the two elastic layers [9]. A further peak, resulting from the resonance of the rail mass on the pad stiffness, occurs in the region 300-500 Hz [10, 11]. It may shift to a higher frequency if the rail pads are stiffer, making it difficult to tell apart from the so-called pinned-pinned resonance at around 1000 Hz [9, 12]. The pinned-pinned resonance corresponds to a standing wave in a discretely supported rail, with half a wavelength equal to the sleeper spacing [13]. Severe vibration of the train-track coupled system can occur if the frequency of excitation due to track irregularities is equal to the pinned-pinned frequency [14]. It should be noted that the pinned-pinned frequency is mainly determined by the fastener spacing rather than the stiffness of the supports but the effect is more significant for fasteners with a

high stiffness [9, 15-17].

Due to the presence of multiple wheels on a rail, the responses from multiple wheel-rail interactions are found to contain additional resonance peaks [15]. An earlier study carried out by Igeland [4] has observed several peaks around 600-800 Hz in the spectrum of wheel-rail interaction forces, for a bogie moving on a discretely supported rail. She attributed this phenomenon to various standing waves in the rail with nodes at the two wheels. To calculate the track response induced by multiple wheels, Wu and Thompson [1] introduced the concepts of an active wheel and passive wheels, finding the total response by superposition. A peak at around 600 Hz was then observed both in the point receptance of a rail with additional passive wheels and in the active wheel-rail contact force [1, 18]. Wu and Thompson [19] investigated in detail the peaks in the spectrum of wheel-rail interaction forces, using a track model with multiple wheels on it. It was shown that four main peaks in the interaction forces occurred in the frequency region 550-1200 Hz, different from the results from a single-wheel model, and the peaks become higher when softer rail pads are used. To explain this phenomenon, the effects of wave reflections between the wheels were qualitatively studied. Subsequently, the formation of short pitch corrugation has been studied [4, 15, 20, 21] by considering the multiple peaks in the wheel-rail interaction force. The effects of rail dampers in suppressing the growth of that rail corrugation were investigated including the multiple wheel-rail interactions [15, 21, 22]. The multiple force peaks found in these studies [15, 20-22] were taken as practical factors affecting corrugation. Ding et al. [23] similarly

investigated the influence of wave reflections between multiple wheels on curve squeal.

To investigate these resonances, the first step is to calculate the receptance of the rail, providing a foundation for dealing with wheel-rail interactions both in the time domain and frequency domain [24]. An infinite Timoshenko beam is often applied to include the effect of shear deformation and rotational inertia of the rail, which become important at frequencies above 500 Hz [25]. A wavenumber-based method was developed by Sheng et al. [26] that can be used to calculate track vibration excited by a high frequency harmonic load moving at high speed. It is noted that the response of this discretely supported model to a harmonic load is not purely harmonic, causing difficulties in dealing with train-track dynamics in the frequency domain [9, 26]. In fact, however, the effect of the discrete supports can be neglected if the frequency of interest does not fall in the vicinity of the pinned-pinned frequency, especially for soft rail pads [14]. By adopting a continuously supported model, the track becomes an invariant system with respect to space, meaning that, when subjected to a moving harmonic load, it will give a stationary response in the moving frame at the frequency of the load [27]. A moving roughness model [1, 18, 19, 22] is often employed to calculate wheel-rail interactions, in which the wheels are assumed to be stationary and irregularities are pulled between the wheels and the rail as a relative excitation [19]. At low frequencies the effect of the moving load becomes important for tracks on soft soil when the train speed approaches the wave speed in the ground [28, 29]. However, these effects are limited to frequencies below 100 Hz.

Recently, peaks in the track vibration in the frequency range from around 400 Hz to 1000 Hz have been once more observed by the authors during several field measurements made on a viaduct with ballastless track. Although these peaks have been observed in several papers, as discussed above, the aim of this study is to investigate the generation mechanism responsible for them in more detail, to give both mathematical and physical insight. To apply the frequency-domain method, a typical model of an infinite Timoshenko beam with continuous supports is adopted for modelling the track system, and its point and transfer receptances are explicitly obtained by a Fourier transform-based method together with the residue theorem. Then, the power spectral densities (PSDs) of the system response are derived analytically. By adopting the concepts of active and passive wheels [1], the multiple peaks in the PSDs of the wheel-rail contact forces are investigated mathematically by extreme value analysis of the response function and from a physical viewpoint based on wave propagation theory. Additionally, the nature of the boundary conditions provided by the wheels is discussed with the concepts of reflection and transmission ratios. Finally, vibration amplifications of the track due to multiple wheels are investigated, and differences between the amplification of wheel-rail contact force and rail vibration are discussed.

2 Receptance of an infinite Timoshenko beam

The rails are usually discretely supported by periodic sleepers or fasteners. However, the effect of the discrete supports can be neglected if the dominant

frequencies do not fall in the vicinity of the pinned-pinned frequency [25, 30], and especially if the rail pads are relatively soft [15-17]. In addition, it was shown by Wu and Thompson [1] that the effects of multiple wheel–rail interactions may also suppress the pinned-pinned resonance. As the shear deformation and rotational inertia of the rail should be considered for frequencies above 500 Hz [25], a continuously supported Timoshenko beam model is used in this study. The response to a stationary harmonic load [27] is used to obtain the point and transfer receptances of the track, initially without wheels mounted on it.

The vibration of a Timoshenko beam is described by the vertical displacement w_r (directed positive downwards) and the rotation angle ϕ_r of the cross-section (clockwise), as shown in Fig. 1. For a stationary harmonic load $Q\mathrm{e}^{\mathrm{i}\omega t}$, with complex-valued amplitude Q and angular frequency ω, the kinetic equations for an infinite Timoshenko beam with continuous supports can be written in the frequency domain in terms of the distance ξ from the load

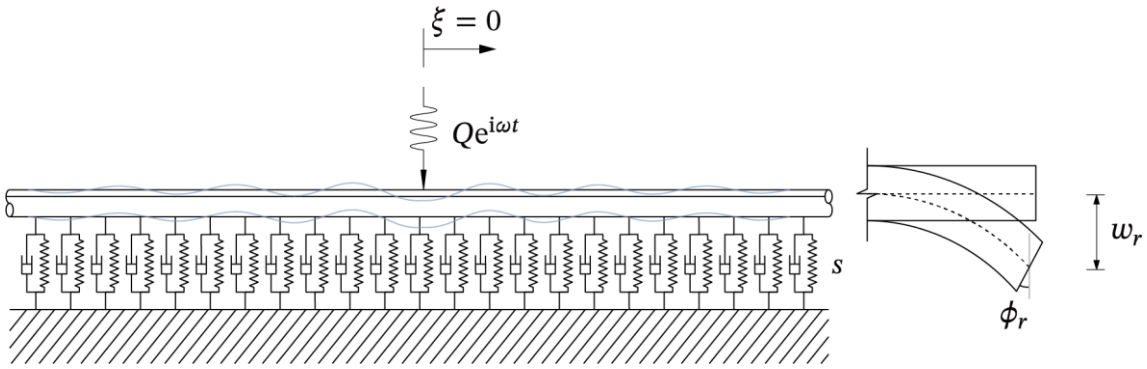

Fig. 1. An infinite Timoshenko beam on an elastic foundation showing the vibration generated by a harmonic load.

$$\begin{cases} GA\kappa\dfrac{\mathrm{d}}{\mathrm{d}\xi}\left(\phi_r-\dfrac{\mathrm{d}w_r}{\mathrm{d}\xi}\right)+(s-\rho A\omega^2)w_r=Q\delta(\xi) \\ GA\kappa\left(\phi_r-\dfrac{\mathrm{d}w_r}{\mathrm{d}\xi}\right)-EI\dfrac{\mathrm{d}^2\phi_r}{\mathrm{d}\xi^2}-\rho I\omega^2\phi_r=0 \end{cases} \tag{1}$$

where w_r and ϕ_r are the complex-valued amplitudes, ρA is the rail mass per unit length, ρI is the rail rotational inertia, EI is the rail bending stiffness, GA is the rail shear stiffness, κ is the rail shear parameter, and s is the support stiffness per unit length. Damping is introduced in the beam and its supports by making the Young's modulus, shear modulus and support stiffness complex with the form $E(1+\mathrm{i}\eta_r)$, $G(1+\mathrm{i}\eta_r)$ and $s(1+\mathrm{i}\eta_s)$ (they are suppressed in the equations for simplicity).

The transfer receptance of the track at a distance ξ from the load can be easily obtained based on a Fourier-transform method [12]

$$H(\xi,\omega)=\frac{1}{2\pi}\int_{-\infty}^{\infty}\frac{M(k)}{N(k)}\mathrm{e}^{-\mathrm{i}k\xi}\mathrm{d}k \tag{2}$$

where

$$M(k)=GA\kappa+EIk^2-\rho I\omega^2 \tag{3}$$

$$N(k)=(GA\kappa k^2+s-\rho A\omega^2)(GA\kappa+EIk^2-\rho I\omega^2)-G^2A^2\kappa^2k^2 \tag{4}$$

The integral in Eq. (2) can be evaluated by using contour integration. For $\xi\geq 0$, the integral is equal to $-2\pi\mathrm{i}$ times the sum of the residues of the poles in the lower half plane, whereas for $\xi<0$, the integral is equal to $2\pi\mathrm{i}$ times the sum of the residues of the poles in the upper half plane. Hence, the receptance is given by

$$H(\xi,\omega)=\begin{cases} -\mathrm{i}\displaystyle\sum_{n=3}^{4}\mathrm{Res}\left[\frac{M(z)}{N(z)}\mathrm{e}^{-\mathrm{i}\xi z},k_n\right]=-\mathrm{i}\left[\frac{M(k_3)\mathrm{e}^{-\mathrm{i}\xi k_3}}{N'(k_3)}+\frac{M(k_4)\mathrm{e}^{-\mathrm{i}\xi k_4}}{N'(k_4)}\right] & (\xi\geq 0) \\ \mathrm{i}\displaystyle\sum_{n=1}^{2}\mathrm{Res}\left[\frac{M(z)}{N(z)}\mathrm{e}^{-\mathrm{i}\xi z},k_n\right]=\mathrm{i}\left[\frac{M(k_1)\mathrm{e}^{-\mathrm{i}\xi k_1}}{N'(k_1)}+\frac{M(k_2)\mathrm{e}^{-\mathrm{i}\xi k_2}}{N'(k_2)}\right] & (\xi<0) \end{cases} \tag{5}$$

where k_n are the zeros of $N(k)$ and $\mathrm{Im}(k_{1,2}) > 0, \mathrm{Im}(k_{3,4}) < 0$. This can be written more simply as

$$H(\xi) = \begin{cases} u_3 \mathrm{e}^{-\mathrm{i}k_3\xi} + u_4 \mathrm{e}^{-\mathrm{i}k_4\xi} & (\xi \geq 0) \\ u_1 \mathrm{e}^{-\mathrm{i}k_1\xi} + u_2 \mathrm{e}^{-\mathrm{i}k_2\xi} & (\xi < 0) \end{cases} \tag{6}$$

where

$$u_j = \begin{cases} -\mathrm{i}M(k_j)/N'(k_j) & (j = 3,4) \\ \mathrm{i}M(k_j)/N'(k_j) & (j = 1,2) \end{cases} \tag{7}$$

Moreover, $u_1 = u_3$, $u_2 = u_4$, $k_1 = -k_3$ and $k_2 = -k_4$. To illustrate the contour integration, use is made of typical parameters given in Table 1 for the rail, which are also applied in the following analysis. It is noted that the support stiffness of $s = 66.67\ \mathrm{MN/m^2}$ corresponds to a vertical fastener stiffness of $40\ \mathrm{MN/m}$ at a fastener spacing of 0.6 m. Damping is introduced in the rail pads and the rail as listed in Table 1. Fig. 2 (a) shows the distribution of the four poles k_n on the complex plane, for a harmonic load at a frequency of 300 Hz. The decay rates for the track waves corresponding to k_3 and k_4 are shown in Fig. 2 (b).

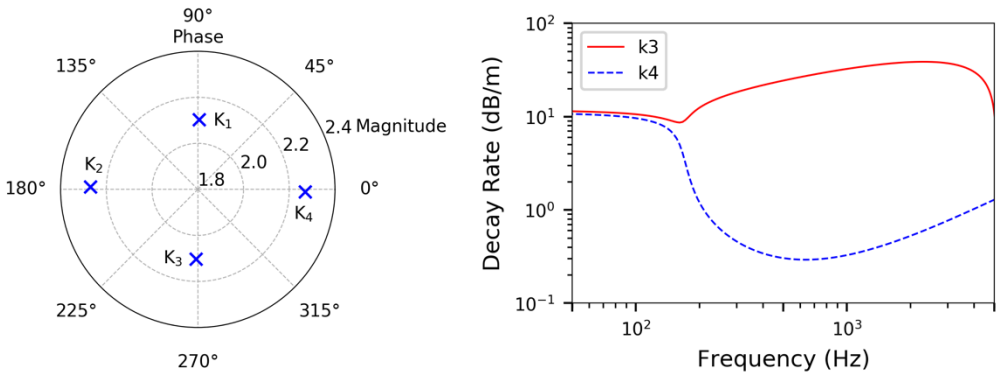

(a) (b)

Fig. 2. Poles of $N(k)$ on the complex plane and decay rates for the track waves using the parameters in Table 1: (a) distribution of four poles at 300 Hz; (b) decay rates.

Table 1. Parameters for railway track based on Timoshenko beam model [12, 31]

Parameter	Definition	Unit	Value
GA	Rail shear stiffness	MN	617
EI	Rail bending stiffness	MNm^2	6.42
η_r	Damping loss factor of rail	/	0.02
ρA	Rail mass per unit length	kg/m	60
ρI	Rail rotational inertia	kgm	0.240
κ	Rail shear parameter	/	0.4
s	Support stiffness per unit length of foundation	$\mathrm{MN/m}^2$	66.67
η_s	Damping loss factor of foundation	/	0.15

As is shown in Fig. 2(a), all the poles are complex-valued, with the real part representing the wavenumber and the imaginary part corresponding to the decay rate. The wave corresponding to k_3 decays exponentially in the whole frequency region, and can be identified as a nearfield wave. In contrast, above the cut-off frequency (170 Hz), the k_4 wave propagates with little attenuation, and plays a dominant role in the track transfer receptance at sufficient distance from the load.

Fig. 3 illustrates the point receptance of the rail and the transfer receptance at $\xi = 2.5$ m. The magnitude of the transfer receptance is far lower than that of the point receptance at frequencies below 200 Hz, due to the high decay rates in this frequency region. A peak is found at around 170 Hz in both point and transfer receptances, corresponding to the resonance of the rail mass bouncing on the pad stiffness which is

also the cut-off frequency for wave propagation [12].

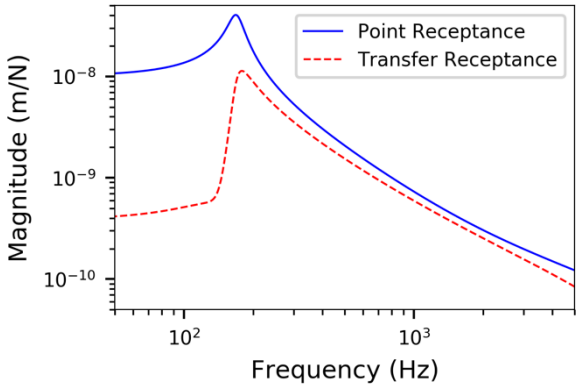

Fig. 3. Magnitudes of the point receptance at $\xi = 0$ and the transfer receptance at $\xi = 2.5$ m.

3 Dynamics of the wheel-track coupled system

In this section, the receptances obtained in Section 2 are employed to derive the spectral density matrices for the response of the track and the wheels (see Fig. 4) excited by random roughness or irregularities. The moving irregularity model is used to solve the wheel-track coupled dynamics, in which irregularities are pulled between the wheels and the rail as a relative excitation.

3.1 Wheel-track coupled model

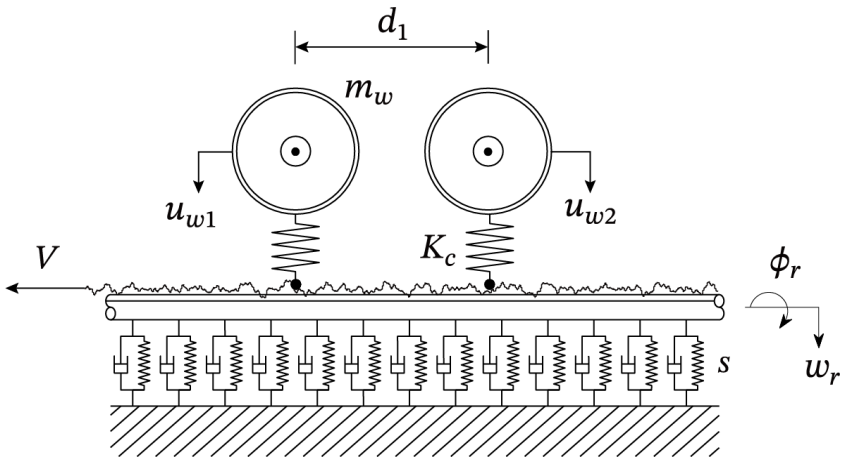

Fig. 4. Two-dimensional model of two wheels supported by an infinite elastic track

represented by a Timoshenko beam.

The investigation is based on the model of a track coupled with two wheels, which represent one bogie, as shown in Fig. 4. The bogie and car body are omitted from the model; this only affects the results at frequencies below about 10 Hz. The wheels are regarded as rigid bodies, and only vibration in the vertical direction is considered. It is noted that, for vertical motion, the rigid model for the wheel is reasonable for frequencies below 1 kHz. At higher frequencies flexible modes in the radial direction occurring above 2 kHz should be considered [12]. Table 2 lists the main parameters used to describe the wheels along with their values that relate to a metro train in Shanghai.

Table 2. Parameters for the wheels used in urban rail transit in Shanghai

Parameter	Definition	Unit	Value
m_w	Mass of the wheel (half wheelset)	kg	894
d_1	Distance between the two wheels of one bogie	m	2.5
K_c	Equivalent vertical stiffness of wheel-track contact per wheel	N/m	1.5×10^9

The wheel-rail contact model is an essential element for analyzing the dynamic performance of the entire system. A linearized contact spring is adopted for simplifying the system as a linear stationary stochastic vibration problem (see Fig. 5), which is reasonable for typical levels of excitation [32]. Thus, the dynamic interaction force at the i-th wheel-rail contact point, f_i, can be determined by

$$f_i = K_c(u_{wi} - u_{ci}) \tag{8}$$

where u_{wi} is the vertical displacement of the i-th wheel; u_{ci} is the displacement of the contact end of the i-th contact spring ($i = 1,2$) and K_c is the linearized contact stiffness.

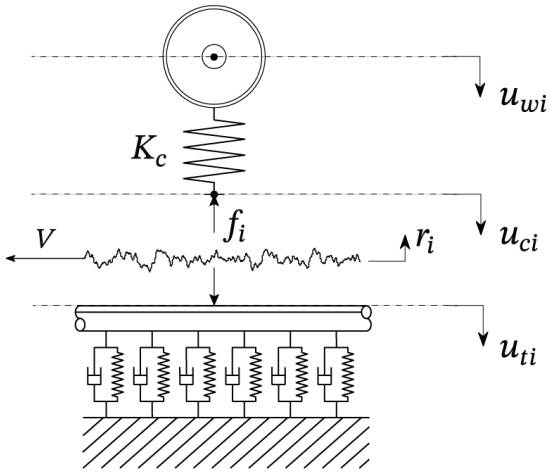

Fig. 5. Schematic diagram for mechanical analysis of the decomposed wheel-rail system.

Only vertical track irregularities are taken into consideration in this study. These are expressed by the US FRA vertical alignment irregularity PSD function $S_r(\Omega)$ [33]

$$S_r(\Omega) = \frac{kA_r\Omega_c^2}{\Omega^2(\Omega^2 + \Omega_c^2)} \tag{9}$$

where Ω represents the spatial angular frequency of track irregularities; k represents the safety factor, which ranges from 0.25 to 1.0; A_r represents the roughness constant; Ω_c represents the cutoff spatial angular frequency. The track irregularity of class 6 is used in this study for illustration purposes with $k = 1$, $A_r = 0.0339\ \text{cm}^2 \cdot \text{rad/m}$, and $\Omega_c = 0.8245\ \text{rad/m}$.

3.2 Frequency response functions of subsystems

To facilitate mechanical analysis, the original coupled model can be decomposed into the wheel-spring subsystem, the irregularity and the track subsystem, as is shown

schematically in Fig. 5. Based on the aforementioned assumptions, the response of wheel-spring subsystem can be determined in the frequency domain as

$$\mathbf{U}_c = -\boldsymbol{\alpha}_0 \mathbf{F}_w \tag{10}$$

in which $\mathbf{U}_c = \{U_{c1} \quad U_{c2}\}^{\mathrm{T}}$ is the displacement vector of contact points on the springs, and $\mathbf{F}_w = \{F_{w1} \quad F_{w2}\}^{\mathrm{T}}$ is the vector of the wheel-rail interaction forces. $\boldsymbol{\alpha}_0$ is defined as the receptance matrix of the wheel-spring subsystem [1]. Since the two wheels are assumed to be unconnected, $\boldsymbol{\alpha}_0$ is a diagonal matrix expressed as

$$\boldsymbol{\alpha}_0 = \mathrm{diag}\{1 \quad 1\} \times \left(\frac{1}{K_c} - \frac{1}{m_w \omega^2}\right) \tag{11}$$

The negative sign in Eq. (10) represents the fact that the forces act upward on the wheels (Fig. 5).

Similarly, the response of the contact points on the track, $\mathbf{U}_t = \{U_{t1} \quad U_{t2}\}^{\mathrm{T}}$, can be written as

$$\mathbf{U}_t = \mathbf{H}_t \mathbf{F}_w \tag{12}$$

where $\mathbf{H}_t$ is the receptance matrix of the track subsystem and can be determined from the point and transfer receptances, Eq. (5), with consideration of the superposition principle

$$\mathbf{H}_t = \begin{bmatrix} H(0) & H(-d_1) \\ H(d_1) & H(0) \end{bmatrix} \tag{13}$$

It should be noted that $\mathbf{H}_t$ is symmetric due to the use of the moving irregularity assumption, in which the effect of load motion on the rail is neglected.

3.3 Solution of coupled system

The track irregularities are assumed to be a spatial stochastic process. If the running

of the wheels is taken into consideration, the irregularities under each contact point become temporal variables, which can be expressed in the frequency domain as

$$\mathbf{R}_w = \{R_1 \quad R_2\}^{\mathrm{T}} \tag{14}$$

To ensure the wheel-rail contact is maintained, the various displacements are related by

$$\mathbf{U}_t - \mathbf{R}_w = \mathbf{U}_c \tag{15}$$

where $\mathbf{R}_w$ is the complex-valued vector of the irregularity input at a certain frequency (positive for an asperity). Substituting Eq. (10) and (12) into Eq. (15), the interaction forces $\mathbf{F}_w$ can be obtained by

$$\mathbf{F}_w = (\boldsymbol{\alpha}_0 + \mathbf{H}_t)^{-1}\mathbf{R}_w = \mathbf{K}_d\mathbf{R}_w \tag{16}$$

where $\mathbf{K}_d$ is a dynamic stiffness matrix, the inverse of the combined receptance matrix, which converts spatial geometric irregularities into equivalent wheel-rail interaction forces

$$\mathbf{K}_d = (\boldsymbol{\alpha}_0 + \mathbf{H}_t)^{-1} \tag{17}$$

The displacement response of the contact points on the track can be easily obtained by substituting Eq. (16) into Eq. (12)

$$\mathbf{U}_t = \mathbf{H}_t\mathbf{K}_d\mathbf{R}_w \tag{18}$$

3.4 Response PSD

The spectral density matrix for the wheel-rail contact force $\mathbf{S}_{\mathbf{f}_w}$ and for the response of the contact points on the track $\mathbf{S}_{\mathbf{U}_t}$ can be expressed as [34]

$$\mathbf{S}_{\mathbf{f}_w} = \lim_{T\to\infty} \frac{\mathbf{F}_w^{*}\mathbf{F}_w^{\mathrm{T}}}{2T} \tag{19}$$

$$\mathbf{S}_{\mathbf{U}_t} = \lim_{T\to\infty} \frac{\mathbf{U}_t^* \mathbf{U}_t^{\mathrm{T}}}{2T} \tag{20}$$

where the superscript * denotes the conjugate and superscript T denotes the transpose operation, and the variable T in the denominator is the duration of the signal that is considered. Substituting Eq. (16) into Eq. (19) and Eq. (18) into Eq. (20), $\mathbf{S}_{\mathbf{f}_w}$ and $\mathbf{S}_{\mathbf{U}_t}$ can be obtained as

$$\mathbf{S}_{\mathbf{f}_w} = \mathbf{K}_d^* \mathbf{S}_r \mathbf{K}_d^{\mathrm{T}} \tag{21}$$

$$\mathbf{S}_{\mathbf{U}_t} = \mathbf{H}_t^* \mathbf{K}_d^* \mathbf{S}_r \mathbf{K}_d^{\mathrm{T}} \mathbf{H}_t^{\mathrm{T}} \tag{22}$$

where $\mathbf{S}_r$ is defined as the spectral density matrix for the irregularities at the contact points, given by

$$\mathbf{S}_r = \lim_{T\to\infty} \frac{\mathbf{R}_w^* \mathbf{R}_w^{\mathrm{T}}}{2T} = \boldsymbol{\mathcal{B}}(\omega, V) \frac{1}{V} S_r\left(\frac{\omega}{V}\right) \tag{23}$$

in which $S_r(\Omega)$ is the spatial-PSD function of track irregularities in Eq. (9); $\boldsymbol{\mathcal{B}}(\omega, V)$ is a phase-lag matrix, describing relationships of time delay among the excitations. The use of the phase-lag matrix allows different types of excitation to be represented. For example, at low frequencies, excitations at the two wheels can be regarded as strictly correlated, and $\boldsymbol{\mathcal{B}}(\omega, V)$ can be expressed as

$$\boldsymbol{\mathcal{B}}(\omega, V) = \begin{bmatrix} 1 & \mathrm{e}^{-\mathrm{i}\frac{\omega}{V}d_1} \\ \mathrm{e}^{\mathrm{i}\frac{\omega}{V}d_1} & 1 \end{bmatrix} \tag{24}$$

In contrast, at high frequencies an uncorrelated excitation model is more reasonable, for which $\boldsymbol{\mathcal{B}}(\omega, V)$ can be obtained as

$$\boldsymbol{\mathcal{B}}(\omega, V) = \mathrm{diag}\{1 \quad 1\} \tag{25}$$

The derivation of Eq. (24) and Eq. (25) can be found in [35]. For the active-passive wheel model which has been developed in [1], the irregularity excitation is only applied

on one wheel at a time. If the first wheel is treated as the active wheel, $\boldsymbol{\mathcal{B}}(\omega, V)$ can be expressed as

$$\boldsymbol{\mathcal{B}}(\omega, V) = \mathrm{diag}\{1 \quad 0\} \tag{26}$$

4 Mechanism analysis

4.1 Influence of additional wheel

The frequency-domain method is first applied to analyze the vibration of the wheel-track coupled system introduced in Section 3. To investigate the generation mechanism of the multiple peaks observed in the spectra of wheel-rail interaction forces [15, 19], the model including active and passive wheel/rail interactions is applied in the following sections, as shown in Fig. 6. Track irregularities are assumed to exist under the left-hand wheel (the active wheel), using the US FRA class 6 spectrum in Eq. (9), and the other wheel is excited only by the rail vibration; this is treated as the passive wheel. Responses of this active-passive wheel model can be easily calculated based on previous derivations in Section 3, in which Eq. (26) should be adopted.

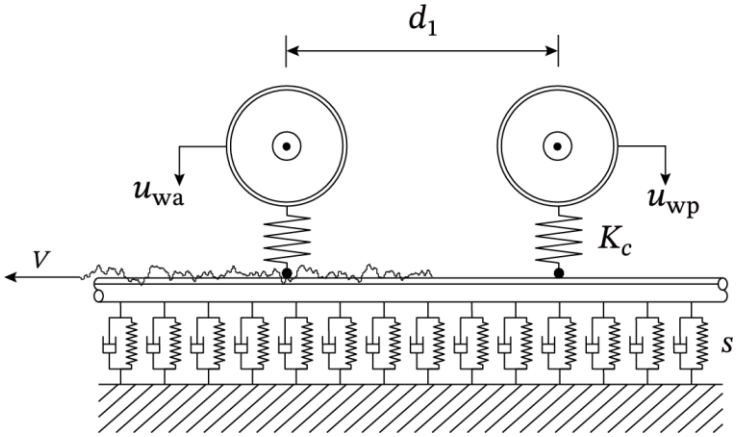

Fig. 6. An infinite Timoshenko beam model of the rail with two wheels with irregularities only existing under the active (left-hand) wheel.

The response PSDs of the active and passive contact forces are presented in Fig. 7 (a), for a passage speed of 40 m/s. As a comparison, the response PSD of wheel-rail contact forces for a single wheel running on the rail at this speed is shown in Fig. 7 (b).

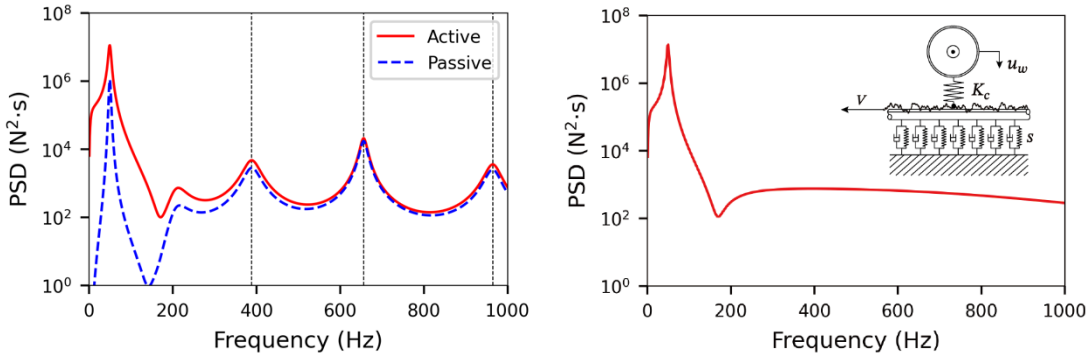

(a) (b)

Fig. 7. PSD functions of wheel-rail contact forces for the system of (a) the active and passive wheels on the rail; (b) a single wheel on the rail.

As can be seen from Fig. 7 (a), there are several peaks in the PSD which can be divided into two categories. In the low frequency region, a strong peak occurs at around 50 Hz that corresponds to the so-called P2 resonance of the wheel mass on the track stiffness [10, 12]. In the frequency range from 400 Hz to 1000 Hz, there are additional peaks, the highest of which occurs at around 656 Hz. In contrast, these additional peaks do not occur in Fig. 7 (b), with only the peak corresponding to the P2 resonance of the wheel on the rail appearing. Therefore, the effects of the additional passive wheel on the rail have changed the pattern of wheel/rail interactions, leading to multiple peaks in the response [1, 18].

4.2 Mathematical reasoning

These multiple peaks can be explained from a mathematical perspective. Assume the active wheel is subjected to a particular component of track irregularities with a constant wavelength. Utilizing the frequency-domain method established above, the interaction forces $\mathbf{F}_w = [F_a \quad F_p]^{\mathrm{T}}$ can be derived from Eq. (16), in which F_a represents contact forces of the active wheel and F_p for the passive wheel. Note that the irregularity under the passive wheel is zero, so the complex-valued vector of the irregularity input can be expressed as $\mathbf{R}_w = [R \quad 0]^{\mathrm{T}}$. By expanding Eq. (16), the active and passive contact forces can then be determined by

$$F_a = \frac{[H(0) + \alpha_0]R}{[H(0) + \alpha_0]^2 - H(d_1)H(-d_1)} \tag{27}$$

$$F_p = \frac{-H(d_1)R}{[H(0) + \alpha_0]^2 - H(d_1)H(-d_1)} \tag{28}$$

The contact forces are complex-valued functions of frequency, especially as the rail receptance $H(\xi)$ is a complex-valued integral, but the contact force magnitude will reach a local maximum if the modulus of the denominator in Eq. (27) or Eq. (28), which is the determinant of the combined receptance matrix, has a local minimum. Fig. 8 gives the modulus of the denominator in the contact forces as a function of frequency.

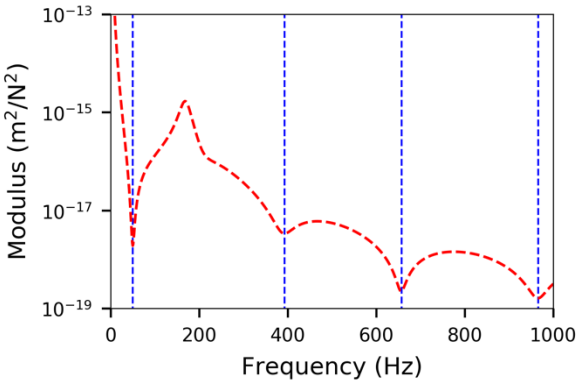

Fig. 8. The determinant of the combined receptance matrix in contact force expressions as a function of frequency.

As expected, the curve has local minima at around 50 Hz, 389 Hz, 656 Hz and 965 Hz, exactly the places where the multiple peaks occur in Fig. 7 (a). This kind of explanation makes sense from a mathematical viewpoint, but it fails to provide a physical interpretation and still cannot answer the question why these functions have local extrema at certain frequencies.

4.3 Wave reflection and transmission at a wheel

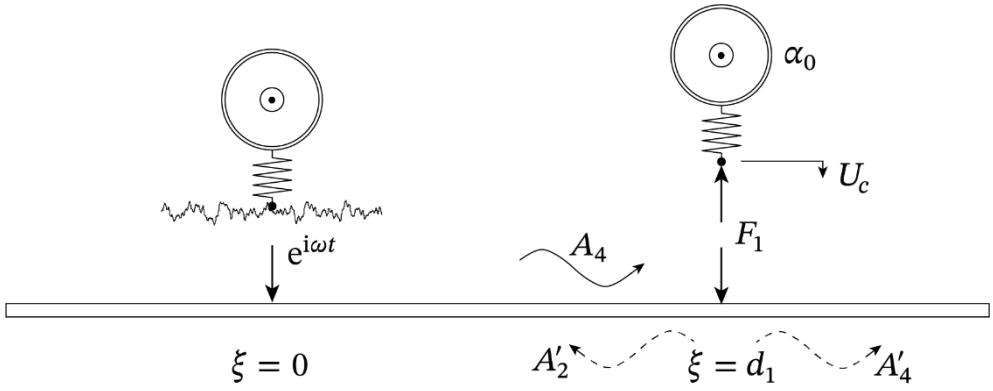

Fig. 9. An infinite beam excited at $\xi = 0$ with an attachment at $\xi = d_1$.

To derive a more physical explanation, the waves propagating in the rail are considered in this Section. Fig. 9 again shows the rail attached to two wheels, one of which is active at $\xi = 0$, excited by irregularity excitation, and the other is passive at $\xi = d_1$. Assume that the active wheel initially generates a unit harmonic force at $\xi = 0$. The total displacement at $\xi = d_1$ is the sum of the incident wave and the response caused by the reaction force F_1, and is equal to the displacement of the passive wheel

$$H(d_1) + F_1 H(0) = U_c = -F_1 \alpha_0 \tag{29}$$

where α_0 is the receptance of the wheel-spring system defined in Eq. (11). Hence

$$F_1 = \frac{-H(d_1)}{\alpha_0 + H(0)} \tag{30}$$

As discussed in Section 2, the incident nearfield wave decays rapidly and so it can be considered negligible after a distance of 2.5 m (at $\xi = d_1$). Therefore, from Eq. (6) the transfer receptance can be written in terms of the incident wave as $H(d_1) \approx u_4 \mathrm{e}^{-\mathrm{i}k_4 d_1} = A_4$, having undergone a phase change $\mathrm{Re}(-k_4)d_1$. The reflected propagating wave is generated by the reaction force F_1, with the amplitude

$$A_2' = F_1 u_2 = \frac{-A_4 u_2}{\alpha_0 + H(0)} \tag{31}$$

at $\xi = d_1$, in which $u_2 = u_4$ is the propagating wave component in the point receptance $H(0)$. The amplitude reflection ratio is given by the ratio of reflected to incident waves

$$r_1 = \frac{A_2'}{A_4} = \frac{-u_2}{\alpha_0 + H(0)} = \frac{-u_4}{\alpha_0 + u_3 + u_4} \tag{32}$$

The phase of the reflection ratio can be written as $\epsilon_1 = \arg(r_1)$.

Unlike a finite beam, a transmitted wave will also propagate beyond the attachment. The total amplitude of the transmitted wave in this region ($\xi > d_1$) is the sum of the incident wave A_4 and the propagating wave A_4' generated by the reaction force. The amplitude transmission ratio can be written as:

$$t_1 = \frac{A_4 + A_4'}{A_4} = 1 - \frac{u_4}{\alpha_0 + u_3 + u_4} \tag{33}$$

Using the same parameters as in Tables 1 and 2, Fig. 10 (a) shows the amplitude reflection ratios for a wheel-spring attachment. Also shown is the result for a grounded spring $\alpha_0 = 1/K_c$. Fig. 10 (b) shows the corresponding transmission ratios.

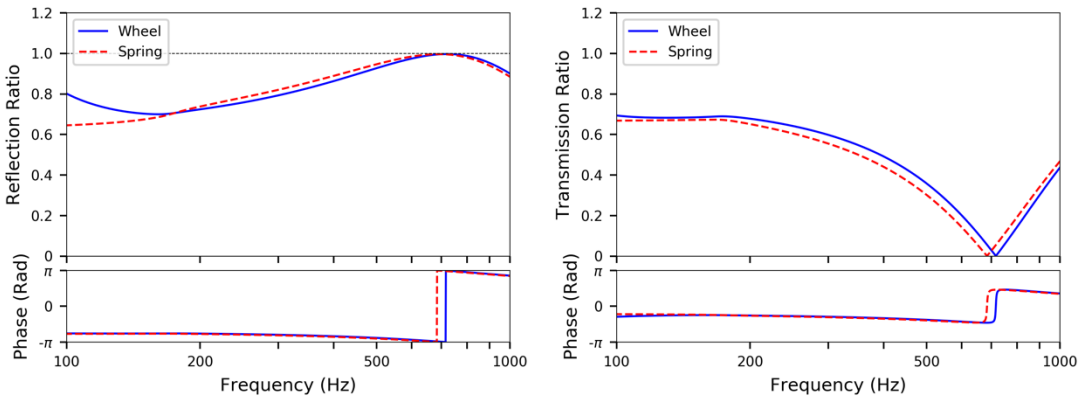

(a) (b)

Fig. 10. Amplitude reflection ratios (a) and transmission ratios (b) for a wheel-spring system and a grounded spring.

The reflection ratio has a magnitude less than 1 at most frequencies (due to energy transmission beyond the wheel) but it tends to 1 at 687 Hz (718 Hz when the wheel mass is included). The transmission coefficient tends to 0 at this frequency, signifying total reflection. The phase of the reflection ratio varies from $-\pi$ to -0.77π and 0.65π to π within the frequency range shown and equals $\pm\pi$ at the frequency at which the transmission coefficient tends to 0.

Fig. 11 shows the magnitudes and phases of the point receptance for the rail $H(0)$, as well as the two wave components u_3 and u_4. At low frequencies, the two wave components have similar magnitudes (as would be found for an Euler-Bernoulli beam) and a phase difference of $\pi/2$. Above the resonance frequency of the rail mass on the stiffness of the elastic support at 168 Hz, the wave component u_3 has a phase of $-\pi$, corresponding to mass-like behaviour, and u_4 has a phase of $-\pi/2$. Above a few hundred Hertz, due to the influence of shear deformation and rotational inertia, the

relative magnitude of wave 3 (the decaying wave) becomes smaller and that of wave 4 becomes larger (compared with an Euler-Bernoulli beam) so that the receptance of the rail becomes dominated by the propagating wave (wave 4) and the phase of the rail receptance tends to $-\pi/2$.

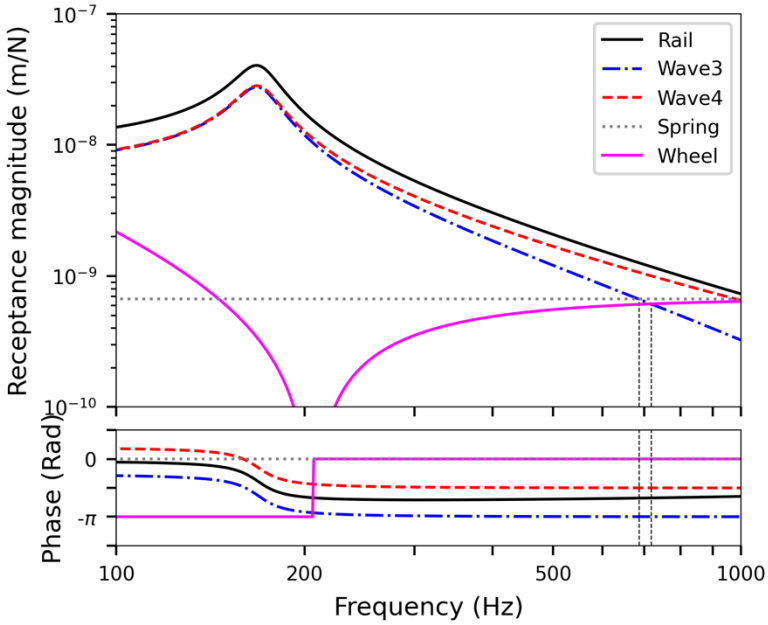

Fig. 11. Magnitudes and phases of point receptance of the rail, the two wave components u_3 and u_4, the wheel-spring system α_0 and the contact spring $1/K_c$.

To clarify the total reflection by the wheel, these receptances are also compared with α_0 for the wheel-spring system and for the grounded spring. At frequencies above 200 Hz, α_0 has a phase of 0, the opposite to u_3. It can be identified that α_0 for the grounded spring and the nearfield wave component u_3 have equal magnitudes at 687 Hz; when the wheel mass is included this occurs at 718 Hz. According to Eq. (32)-(33), when $\alpha_0 = -u_3$, the amplitude reflection ratio r_1 will be -1, and the transmission ratio t_1 will equal to 0, which signifies that total reflection occurs, and the energy is

constrained between the two wheels.

4.4 Explanation of force peaks based on wave propagation theory

When the reflected wave in Eq. (31), with amplitude A_2', arrives back at $\xi = 0$, its amplitude becomes $A_2'' = A_2' \mathrm{e}^{\mathrm{i}k_2 d_1}$ and it will have experienced a further phase change of $\mathrm{Re}(k_2)d_1$. A similar process to that described above can then give the amplitude reflection ratio at the active wheel at $\xi = 0$, which can be written as

$$r_2 = \frac{A_4''}{A_2''} = \frac{-u_4}{\alpha_0 + H(0)} = \frac{-u_4}{\alpha_0 + u_3 + u_4} = r_1 \tag{34}$$

where A_4'' is the amplitude of wave 4 at $\xi = 0$ after the second reflection. The phase of this reflection ratio can be written as $\epsilon_2 = \arg(r_2)$.

According to the phase closure principle [36], resonance will occur if $\epsilon_1 + \mathrm{Re}(-k_4)d_1 + \epsilon_2 + \mathrm{Re}(k_2)d_1 = 2n\pi$, for integer values of n. As $r_1 = r_2$ and $k_2 = -k_4$, the condition becomes $\epsilon_1 + \mathrm{Re}(k_2)d_1 = n\pi$.

Similar to Eq. (30), the reaction force at the active wheel can be written as

$$F_2 = \frac{-A_2''}{\alpha_0 + H(0)} \tag{35}$$

Expanding the expression for A_2'' from above,

$$F_2 = \frac{-u_4 \mathrm{e}^{-\mathrm{i}k_4 d_1} r_1 \mathrm{e}^{\mathrm{i}k_2 d_1}}{\alpha_0 + H(0)} = r_2 \mathrm{e}^{-\mathrm{i}k_4 d_1} r_1 \mathrm{e}^{\mathrm{i}k_2 d_1} \tag{36}$$

Denoting the ratio of this reaction force to the initial (unit) force by η, it can be found that the phase of η is the same as that given in the phase closure principle

$$\arg(\eta) = \epsilon_1 + \mathrm{Re}(-k_4)d_1 + \epsilon_2 + \mathrm{Re}(k_2)d_1 \tag{37}$$

This implies that, when satisfying the phase closure principle, the reaction force will be in phase with the initial force and the excitation will be intensified. Fig. 12 shows the

magnitudes and phases of the coefficient η for an infinite track excited at $\xi = 0$ with a passive wheel at $\xi = d_1$ and the case with a grounded spring at $\xi = d_1$.

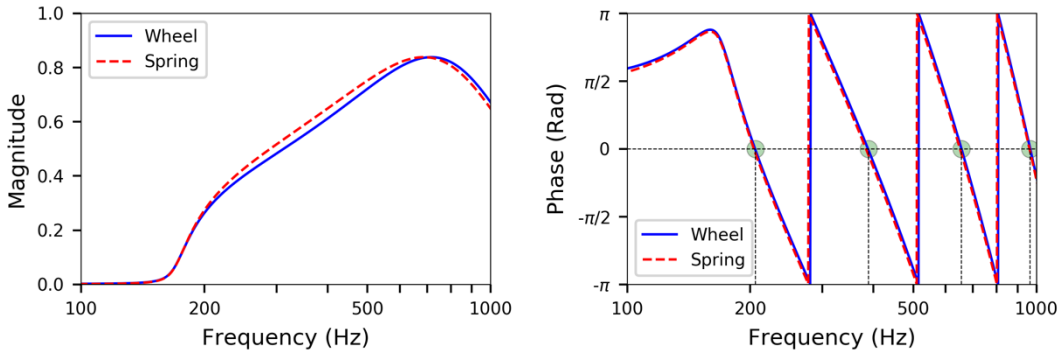

(a) (b)

Fig. 12. The magnitudes and phases of the coefficient η for an infinite beam excited at $\xi = 0$ with a passive wheel at $\xi = d_1$ and the case with a grounded spring at $\xi = d_1$: (a) magnitude; (b) phase.

It can be seen that the magnitude of η is less than 1, due to the effect of wave attenuation and the influence of the wheel and contact receptances in α_0. The phase of η reaches $2n\pi$ at around 200 Hz, 389 Hz, 656 Hz and 965 Hz, where the peaks were found in Fig. 7 (a). The reflected wave will continue to propagate and get reflected between the two wheels. As long as it is in phase with the initial irregularity, the excitation will be continuously intensified, leading to the peaks in the response. The total force at the active wheel due to an infinite number of reflections becomes

$$F_{\text{total}} = \sum_{n=0}^{\infty} \eta^n F_0 = \frac{F_0}{1-\eta} \tag{38}$$

which is equivalent to Eq. (27). It is noted that the velocity of the vehicle has no influence on the frequencies at which the multiple peaks occur, because $\arg(\eta)$ is

independent of the vehicle velocity due to the moving irregularity assumption. However, it may affect the magnitude of the peaks in the response PSD, for the irregularity excitation depends on the vehicle velocity according to Eq. (23).

To investigate the wave interference phenomenon further, the presented frequency-domain method is applied to analyze a track coupled with four wheels, representing a pair of bogies at the adjacent ends of two vehicles. The uncorrelated irregularity excitation is assumed for each wheel, and the PSDs of the vertical contact forces from the first and second wheels are shown in Fig. 13, for a passage speed of 40 m/s. The distance between wheels 2 and 3, $d_2 = 7.1$ m; all other parameters are the same as above.

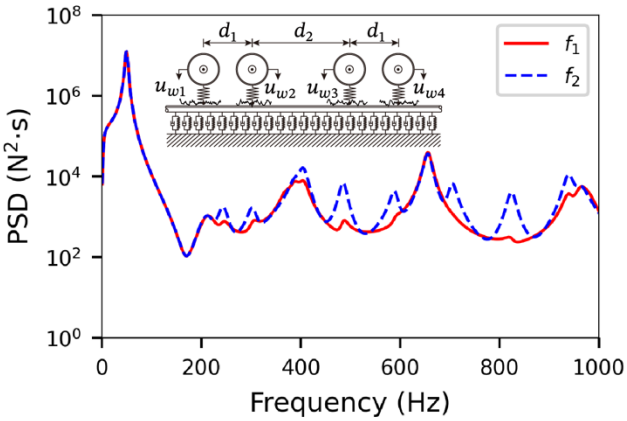

Fig. 13. PSD functions of the first and the second wheel-rail contact forces for the system of four wheels on the rail with uncorrelated irregularity excitation.

In Fig. 13, multiple response peaks can be observed at frequencies above 200 Hz in the contact forces, which broadly resembles the results in Fig. 7 (a). Moreover, the force at the second wheel (the dashed line) contains more peaks than the first wheel (the solid line). Due to the decay rate of the wave propagation, the middle wheels, e.g., the

second wheel, will receive more reflected waves from the adjacent wheels than the outer wheels, e.g., the first wheel. Therefore, more peaks are observed in the dashed line.

5 Vibration amplification due to multiple wheels

To investigate further the amplification effect on the track response due to multiple wheels, Fig. 14 shows the ratio of the total interaction force at the active wheel between the cases with and without an additional passive wheel on the track. Also shown is the ratio of the rail dynamic stiffness (the inverse of the rail point receptance) and the rail displacement response at the active wheel.

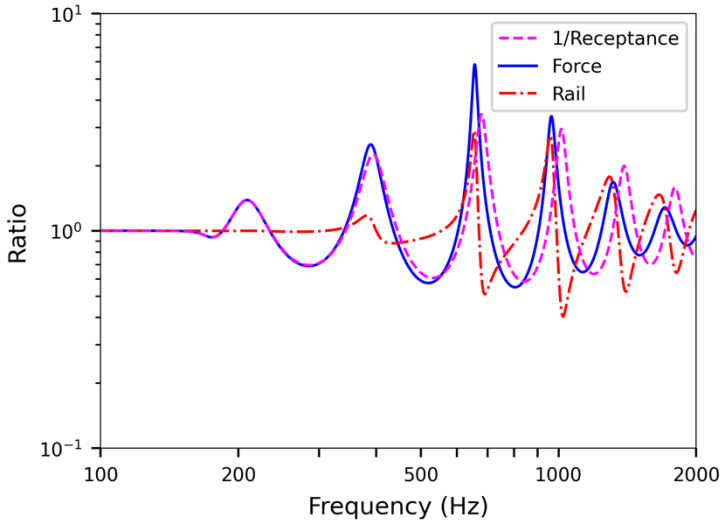

Fig. 14. Ratios of 1/receptance, contact force and rail displacement response at the contact for the cases with and without a passive wheel at 2.5 m from the excitation point.

Due to presence of multiple wheels on the rail, each of these ratios has a series of peaks that can be associated with wave reflections between the wheels, but the amplification for the rail vibration is not as great as that for the interaction force.

Moreover, it is seen that these peaks occur at slightly different frequencies in the three curves. The first few peaks in the force spectrum are close to those found in the dynamic stiffness, whereas at high frequency the peaks in the rail displacement spectrum correspond to the dips in the dynamic stiffness, i.e., local maxima of the rail receptance.

To explain this, it can be noted that the contact force at the active wheel can be written as

$$F_a = \frac{R}{\alpha_0 + H_0^w} \tag{39}$$

and the rail displacement at the contact point as

$$w_{\mathrm{ra}} = F_a H_0^w = \frac{R H_0^w}{\alpha_0 + H_0^w} \tag{40}$$

where R is the complex-valued amplitude of the irregularity input and H_0^w is the receptance of the rail with added passive wheel

$$H_0^w = H(0) - \frac{H(d_1)H(-d_1)}{\alpha_0 + H(0)} \tag{41}$$

At low frequencies $|\alpha_0| \ll |H_0^w|$ leading to $F_a \approx R/H_0^w$ and $w_{\mathrm{ra}} \approx R$, whereas at high frequencies $|\alpha_0| \gg |H_0^w|$ leading to $F_a \approx R/\alpha_0$ and $w_{\mathrm{ra}} \approx R H_0^w/\alpha_0$.

At 200 Hz the rail displacement response is unaffected by the additional wheel and the ratio in Fig. 14 is equal to 1. At this frequency the wheel and contact spring receptances have equal magnitude and opposite phase (see Fig. 11), so $\alpha_0 = 0$ and from Eq. (40) the rail response is equal to the roughness despite the addition of the passive wheel (which acts as a pinned constraint).

If the amplitude reflection ratio is equal to –1, resonance will occur when $\mathrm{Re}(k_2)d_1 = n\pi$, similar to a simply supported finite beam [36]. Frequencies at which the wavenumber $\mathrm{Re}(k_2) = n\pi/d_1$ can be identified in Fig. 15 and are listed in Table

3 along with the peak frequencies from the three curves in Fig. 14.

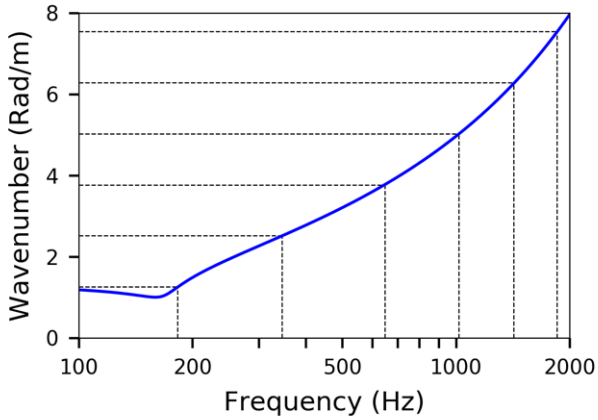

Fig. 15. Real part of propagating wavenumber, with horizontal lines at $n\pi/d_1$.

Table 3. Peak frequencies from Fig. 14 and corresponding to n half wavelengths from Fig. 15.

n	n half wavelengths	1/receptance	Contact force	Rail response
1	183 Hz	208 Hz	208 Hz	/
2	346 Hz	393 Hz	389 Hz	380 Hz
3	647 Hz	679 Hz	656 Hz	652 Hz
4	1018 Hz	1015 Hz	965 Hz	955 Hz
5	1422 Hz	1392 Hz	1318 Hz	1287 Hz

The frequencies identified from Fig. 15 are lower than the actual peak frequencies for $n = 1, 2$ and higher for $n = 4, 5$, but they are approximately equal for $n = 3$, which is the peak closest to 718 Hz, at which total reflection occurs.

Unlike phase closure on a finite beam, as the beam is infinite there is transmission of energy beyond the attachment, as seen in Fig. 10. This acts as a form of radiation damping to limit the magnitude of the peaks. However, if $\alpha_0 = -u_3$ (identified at 718

Hz in Fig. 11) the transmitted wave amplitude tends to 0 (see Eq. (33)) and the energy is constrained between the two wheels. From Fig. 14 it can be seen that there is maximum amplification at the peak around 650 Hz, at least in terms of the force. This is also affected by the track decay rate which has a broad minimum between 500 and 1000 Hz.

6 Conclusions

This study has investigated the generation mechanism of multiple peaks in the rail vibration spectra in the frequency region 400-1000 Hz. A frequency-domain method has been adopted to calculate the PSD responses of the wheel-track coupled system excited by stochastic irregularities. The track is modelled as an infinite Timoshenko beam with continuous supports. Based on the residue theorem, the point and transfer receptances of the rail are explicitly determined using a Fourier transform-based method.

The results from the analytical wheel-track dynamic interaction model show the multiple peaks in the responses of the system, from around 400 Hz to 1000 Hz, occur with the presence of multiple wheels on the rail. It can be explained through extreme value analysis where the determinant of the combined dynamic stiffness matrix has local minima. The peaks in the interaction force and rail vibration can be identified using the 'phase closure principle' which relates the modes of a finite structure to propagating waves within it. However, the peaks found in the present case do not correspond simply to an integer number of half wavelengths between adjacent wheels.

It has been identified that the boundary conditions introduced by the wheels do not

give a reflection with a phase change of 0 or π, as would be the case for e.g. a simply supported finite beam, which would lead to a mode shape with an integer number of half wavelengths. By studying the amplitude reflection ratio for waves incident on the discontinuity caused by a wheel, it is shown that the phase change varies with frequency.

As the rail is actually infinite, there is transmission of energy beyond the region bounded by the pair of wheels. The amplitude transmission ratio shows the proportion of the incident wave that is transmitted. A frequency can be identified at which total reflection occurs and the energy is constrained between the two wheels; for the current parameters this occurs at around 700 Hz which is close to the highest peak in the interaction force.

Acknowledgements

The study was supported by the National Natural Science Foundation of China (grant numbers 51878501 and 51778495).

References

[1] T.X. Wu, D.J. Thompson, Vibration analysis of railway track with multiple wheels on the rail, J. Sound Vibr., 239 (2001) 69-97.
[2] M. Sun, X.S. Fang, D.X. Mao, X. Wang, Y. Li, Broadband acoustic ventilation barriers, Phys. Rev. Appl., 13 (2020), Article 044028.
[3] X. Wang, D. Mao, W. Yu, Z. Jiang, Acoustic performance of balconies having inhomogeneous ceiling surfaces on a roadside building facade, Building and Environment, 93 (2015) 1-8.
[4] A. Igeland, Railhead corrugation growth explained by dynamic interaction between track and bogie wheelsets, Proceedings of the Institution of Mechanical Engineers Part F-Journal of Rail and Rapid Transit, 210 (1996) 11-20.
[5] J.L. Escalona, H. Sugiyama, A.A. Shabana, Modelling of structural flexiblity in multibody railroad vehicle systems, Veh. Syst. Dyn., 51 (2013) 1027-1058.
[6] T. Tomioka, T. Takigami, Reduction of bending vibration in railway vehicle carbodies using carbody–bogie dynamic interaction, Veh. Syst. Dyn., 48 (2010) 467-486.
[7] P. Vila, J. Fayos, L. Baeza, Simulation of the evolution of rail corrugation using a rotating flexible wheelset model, Veh. Syst. Dyn., 49 (2011) 1749-1769.
[8] X.Y. Zhang, D.J. Thompson, Q. Li, D. Kostovasilis, M.G.R. Toward, G. Squicciarini, J. Ryue, A model of a discretely supported railway track based on a 2.5d finite element approach, J. Sound Vibr., 438 (2019) 153-174.
[9] X. Sheng, M.H. Li, Propagation constants of railway tracks as a periodic structure,

J. Sound Vibr., 299 (2007) 1114-1123.
[10] Q. Li, D.J. Wu, Analysis of the dominant vibration frequencies of rail bridges for structure-borne noise using a power flow method, J. Sound Vibr., 332 (2013) 4153-4163.
[11] N. Vincent, D.J. Thompson, Track dynamic behavior at high-frequencies .2. Experimental results and comparisons with theory, Veh. Syst. Dyn., 24 (1995) 100-114.
[12] D. Thompson, Railway noise and vibration: Mechanisms, modelling and means of control, Elsevier, Oxford, 2008.
[13] X.Y. Zhang, D. Thompson, X.Z. Sheng, Differences between euler-bernoulli and timoshenko beam formulations for calculating the effects of moving loads on a periodically supported beam, J. Sound Vibr., 481 (2020), Article 115432.
[14] J.C.O. Nielsen, A. Igeland, Vertical dynamic interaction between train and track - influence of wheel and track imperfections, J. Sound Vibr., 187 (1995) 825-839.
[15] G. Fang, Y. Wang, Z. Peng, T. Wu, Theoretical investigation into the formation mechanism and mitigation measures of short pitch rail corrugation in resilient tracks of metros, Proceedings of the Institution of Mechanical Engineers, Part F: Journal of Rail and Rapid Transit, 232 (2018) 2260-2271.
[16] J. Egana, J. Vinolas, M. Seco, Investigation of the influence of rail pad stiffness on rail corrugation on a transit system, Wear, 261 (2006) 216-224.
[17] H. Ilias, The influence of railpad stiffness on wheelset/track interaction and corrugation growth, J. Sound Vibr., 227 (1999) 935-948.
[18] T. Wu, D. Thompson, The effects on railway rolling noise of wave reflections in the rail and support stiffening due to the presence of multiple wheels, Applied Acoustics, 62 (2001) 1249-1266.
[19] T. Wu, D. Thompson, Behaviour of the normal contact force under multiple wheel/rail interaction, Veh. Syst. Dyn., 37 (2002) 157-174.
[20] T. Wu, D. Thompson, An investigation into rail corrugation due to micro-slip under multiple wheel/rail interactions, Wear, 258 (2005) 1115-1125.
[21] Y. Wang, T. Wu, The growth and mitigation of rail corrugation due to vibrational interference between moving wheels and resilient track, Veh. Syst. Dyn., 58 (2020) 1257-1284.
[22] T.X. Wu, Y.R. Wang, Modeling of wheel-track interaction with rail vibration damper and its application for suppressing short pitch rail corrugation, in: J.C.O. Nielsen, et al. (Eds.) Proceedings of 11th International Workshop on Railway Noise (IWRN), Uddevalla, Sweden, 9-13 September 2013, Notes on Numerical Fluid Mechanics & Multidisciplinary Design 126 (2015) pp. 361-368.
[23] B. Ding, G. Squicciarini, D. Thompson, Effect of rail dynamics on curve squeal under constant friction conditions, J. Sound Vibr., 442 (2019) 183-199.
[24] X. Sheng, T. Zhong, Y. Li, Vibration and sound radiation of slab high-speed railway tracks subject to a moving harmonic load, J. Sound Vibr., 395 (2017) 160-186.
[25] K.L. Knothe, S.L. Grassie, Modeling of railway track and vehicle track interaction at high-frequencies, Veh. Syst. Dyn., 22 (1993) 209-262.
[26] X. Sheng, C.J.C. Jones, D.J. Thompson, Responses of infinite periodic structures to moving or stationary harmonic loads, J. Sound Vibr., 282 (2005) 125-149.
[27] X. Sheng, Generalization of the fourier transform-based method for calculating the response of a periodic railway track subject to a moving harmonic load, Journal of Modern Transportation, 23 (2015) 12-29.
[28] L. Auersch, The effect of critically moving loads on the vibrations of soft soils and isolated railway tracks, J. Sound Vibr., 310 (2008) 587-607.
[29] G. Lombaert, G. Degrande, Ground-borne vibration due to static and dynamic axle loads of intercity and high-speed trains, J. Sound Vibr., 319 (2009) 1036-1066.
[30] S.L. Grassie, R.W. Gregory, D. Harrison, K.L. Johnson, The dynamic response of railway track to high frequency vertical excitation, Journal of Mechanical Engineering Science, 24 (1982) 77-90.
[31] Q. Li, D.J. Thompson, Prediction of rail and bridge noise arising from concrete railway viaducts by using a multilayer rail fastener model and a wavenumber domain method, Proceedings of the Institution of Mechanical Engineers, Part F: Journal of Rail and Rapid Transit, 232 (2018) 1326-1346.

[32] T. Wu, D. Thompson, Theoretical investigation of wheel/rail non-linear interaction due to roughness excitation, Veh. Syst. Dyn., 34 (2000) 261-282.
[33] V. Garg, R.V. Dukkipati, Dynamics of railway vehicle systems, Elsevier, Toronto, 2012.
[34] A.V. Oppenheim, G.C. Verghese, Signals, systems and inference, Pearson, Boston, 2015.
[35] S.M. Lei, Y.J. Ge, Q. Li, Effect and its mechanism of spatial coherence of track irregularity on dynamic responses of railway vehicles, Mech. Syst. Signal Proc., 145 (2020), Article 106957.
[36] D. Mead, Waves and modes in finite beams: Application of the phase-closure principle, J. Sound Vibr., 171 (1994) 695-702.